Theory of relativistic photoemission for correlated magnetic alloys: LSDA+DMFT study of the electronic structure of Ni_xPd_{1-x}

J. Braun,[1] J. Minár,[1] F. Matthes,[2] C. M. Schneider,[2] and H. Ebert[1]
[1]*Department Chemie/Phys. Chemie, Ludwig-Maximilians-Universität München, 81377 München, Germany*
[2]*Institut für Festkörperforschung IFF-9, Forschungszentrum Jülich, 52425 Jülich, Germany*
(Received 30 April 2010; published 13 July 2010)

Electronic correlations play an important role in determining the properties of solid state systems, in particular, in the presence of narrow bands. In intermetallic alloys the strength of correlation effects and, thus, the details of the electronic structure depend on the concentration of the constituents, their interactions, and the degree of chemical order. Although the electronic structure of such a system can be conveniently studied by photoelectron spectroscopy, the interpretation of the spectra is nontrivial. To enable a quantitative analysis of chemically disordered systems showing correlation effects in photoemission spectroscopy we therefore incorporate dynamical mean-field theory in the fully relativistic version of layer-Korringa-Kohn-Rostoker theory and treat the results within the relativistic one-step model of photoemission generalized to the magnetic alloy case. Our ansatz allows the study of complex layered structures like thin films and multilayers and an almost naturally incorporation of a realistic surface barrier potential. We apply our theory to photoemission data of the magnetic alloy system $Ni_xPd_{1-x}(001)$ and demonstrating that state-of-the-art photoemission theory is required to deal with this complex system. The comparison over a large alloy concentration range provides us with a means to disentangle the influence of alloying and correlation effects.

DOI: 10.1103/PhysRevB.82.024411 PACS number(s): 75.70.Rf, 73.20.−r, 75.50.Bb, 79.60.−i

I. INTRODUCTION

Ferromagnetic alloys and specifically binary ones have focused a high level of scientific activity over the last decades. This is due to the unique possibility these materials offer to tune the magnetic properties such as the magnetic moment, Curie temperature or magnetocrystalline anisotropy over a wide range. The binary alloy FeCo shows a magnetic moment higher than the ones of its constituents at a Co concentration of ~20%.[1] The magneto-optical effects in transition metal ferromagnets are considerably enhanced by alloying with elements with large spin-orbit coupling, such as Pd or Pt.[2,3] Intermetallic compounds with lanthanides are known for their superb hard magnetic properties.[4]

These fascinating properties seem to be very promising for further experimental and theoretical investigations. Due to this fact it is not surprising that interest in scientific investigations on magnetic alloys has continued up to now. A true material design relevant for technological applications is intimately connected with a detailed understanding of the surface and interface electronic structure of these systems. Given the complexity of the problem, it is reasonable to start with relatively simple systems, such as binary compounds. Especially the alloy of the isoelectronic elements nickel and palladium is an ideal candidate to demonstrate and challenge the capability of modern calculational concepts to perform quantitative photoemission analysis. The challenge lies in the demand to successfully combine techniques that allow treating in a fully relativistic mode the aspects of chemical disorder and correlation effects of 3*d* bands and to incorporate this in a one-step photoemission model.

The bulk Ni_xPd_{1-x} alloy system is fully miscible and crystallizes in the face-centered cubic lattice structure.[5] Mössbauer measurements at the bulk alloy material indicated ferromagnetic ordering for any nickel concentration larger than 2%.[6] For our studies, we prepared Ni_xPd_{1-x} alloy films on a $Cu_3Au(100)$ substrate with a thickness of 15 monolayers (ML). Ultrathin films of Ni_xPd_{1-x} on Cu(100)[7] and $Cu_3Au(100)$ (Ref. 8) exhibit an inverse spin-reorientation transition, as it is also known for ultrathin Ni films on Cu(100).[9,10] In addition, within a certain thickness range the orientation of the magnetization direction can be controlled by the alloy composition. In this case, the magnetoelastic anisotropy plays a seminal role in the competition of the different contributions to the magnetic anisotropy. It's magnitude and sign can be adjusted via the lattice mismatch between alloy film and substrate.[8] As magnetism and the electronic band structure properties are always interconnected, a detailed knowledge of the electronic band structure may help to deepen the understanding of the contributions to the magnetoelastic anisotropy. Involved in the magnetoelastic anisotropy and in addition an interesting property of the Ni_xPd_{1-x} alloy system is the size of spin-orbit coupling. Although one cannot state a single value for the spin-orbit coupling, because it changes as a function of the position in the Brillouin zone, one may assume in general that its strength increases when the content of palladium is enlarged in the alloy. For the *d*-like bands along the Δ-direction, we find averaged values of 0.1 eV[11] and 0.3 eV[12] for Ni and Pd, respectively. Therefore, the Ni_xPd_{1-x} system allows us to study the continuous change of the spin-orbit coupling and its implication on the electronic band structure e.g., by its influence on hybridization effects. One has to be aware, however, that the Ni_xPd_{1-x} alloy system introduces two complications for the evaluation of the photoemission data. One is the surface roughness of the Ni_xPd_{1-x} films that depends on the alloy composition due to the different lattice mismatch between film and substrate. Pronounced intensity oscillations of a diffracted electron beam recorded during film growth indicated a good layer-by-layer growth for $Ni_{0.35}Pd_{0.65}$ on $Cu_3Au(100)$

that deteriorates for higher or lower Ni concentrations.[7] A rough surface contributes to breaking the momentum conservation in the photoemission process and leads to a smearing of the photoelectron spectra. The second complication stems from the unknown segregation effect at the surface. Dynamical low-energy electron diffraction studies at the (100) surface of a $Ni_{0.50}Pd_{0.50}$ single crystal alloy gave evidence for an oscillatory segregation profile within the first three surface layers.[13] Its possible implication, e.g., for a proper description of the surface in the one-step photoemission model should be considered when evaluating the photoemission data. Another related point is the consequence for a proper modeling of the alloy film for the density-functional theory (DFT) simulations, as the real surface composition may differ from the measured bulk composition. Important in this discussion may be also the escape depth of the measured photoelectrons that will vary with the photon excitation energy.

Experimentally, the interesting valence band region around the Fermi energy is accessible by means of ultraviolet photoemission spectroscopy (PES)[14] and inverse photoemission spectroscopy (IPE).[15] It is widely accepted to interpret a measured photoemission spectrum by referring to the results of band structure calculations that are based on DFT and the local spin density approximation (LSDA).[16,17] Provided that the electronic and geometric structure is known, some basic spectral features can be explained and a qualitative understanding may be gained. To achieve a reliable interpretation of the experimental spectra, however, it is inevitable to deal quantitatively with the following points. First of all, the wave vector and energy dependence of the transition-matrix elements has to be accounted for. These dependencies are known to be important and actually cannot be neglected. They result from strong multiple-scattering processes which dominate the electron dynamics in the low-energy regime of typically 1–200 eV.[18] The transition-matrix elements also include the effects of selection rules. Last but not least, a realistic description of the surface barrier is essential for a quantitative description of surface states and resonances in simple metals but also in more complex structures such as thin films and multilayers.

The most successful theoretical approach to deal with photoemission is the so-called one-step model as originally proposed by Pendry and co-workers.[18–20] A review on the recent developments and refinements[21] of the approach can be found in Ref. 22 and 23. The main idea of the one-step model is to describe the actual excitation process, the transport of the photoelectron to the crystal surface as well as the escape into the vacuum[24] as a single quantum-mechanically coherent process including all multiple-scattering events. Within this model self-energy corrections, which give rise to damping in the quasiparticle spectrum, are properly included in both the initial and the final states. This for example allows for transitions into evanescent band gap states decaying exponentially into the solid. Similarly the assumption of a finite lifetime for the initial states gives the opportunity to calculate photoemission intensities from surface states and resonances. Treating the initial and final states within the fully relativistic version of layer Korringa-Kohn-Rostoker (KKR) theory,[25] it is a straight forward task to design complex layered structures such as thin films and multilayers within the photoemission theory. Furthermore, the surface described by a barrier potential can be easily included into the multiple-scattering formalism as an additional layer. A realistic surface barrier model which shows the correct asymptotic behavior has been introduced, for example, by Rundgren and Malmström.[26] Here, we present the new version of the fully relativistic one-step model, which is a straightforward generalization of the original work on disordered alloys of Durham and Ginatempo[27,28] for magnetic alloys. The paper is organized as follows. In Sec. II, we present the fully relativistic photoemission theory for magnetic alloys. In Sec. III, we discuss the experimental and computational details. Sec. IV is devoted to our experimental and theoretical results. A summary is given in Sec. V.

II. FULLY RELATIVISTIC ONE-STEP MODEL OF PHOTOEMISSION FOR ALLOYS

A. General considerations

We start our considerations by a discussion of Pendry's formula for the photocurrent which defines the one-step model of PES:[19]

$$I^{\mathrm{PES}} \propto \mathrm{Im}\langle \epsilon_f, \mathbf{k}_\parallel | G_2^+ \Delta G_1^+ \Delta^\dagger G_2^- | \epsilon_f, \mathbf{k}_\parallel \rangle. \tag{1}$$

The expression can be derived from Fermi's golden rule for the transition probability per unit time.[29] Consequently, I^{PES} denotes the elastic part of the photocurrent. Vertex renormalizations are neglected. This excludes inelastic energy losses and corresponding quantum-mechanical interference terms.[19,29,30] Furthermore, the interaction of the outgoing photoelectron with the rest system is not taken into account. This "sudden approximation" is expected to be justified for not too small photon energies. We consider an energy-, angle-, and spin-resolved photoemission experiment. The state of the photoelectron at the detector is written as $|\epsilon_f, \mathbf{k}_\parallel\rangle$, where $\mathbf{k}_\parallel$ is the component of the wave vector parallel to the surface, and ϵ_f is the kinetic energy of the photoelectron. The spin character of the photoelectron is implicit included in $|\epsilon_f, \mathbf{k}_\parallel\rangle$ which is understood as a four-component Dirac spinor. The advanced Green function G_2^- in Eq. (1) characterizes the scattering properties of the material at the final-state energy $E_2 \equiv \epsilon_f$. Via $|\Psi_f\rangle = G_2^- |\epsilon_f, \mathbf{k}_\parallel\rangle$ all multiple-scattering corrections are formally included. For an appropriate description of the photoemission process we must ensure the correct asymptotic behavior of $\Psi_f(\mathbf{r})$ beyond the crystal surface, i.e., a single outgoing plane wave characterized by ϵ_f and $\mathbf{k}_\parallel$. Furthermore, the damping of the final state due to the imaginary part of the inner potential $iV_{0i}(E_2)$ must be taken into account. We thus construct the final state within spin-polarized low-energy electron diffraction (SPLEED) theory considering a single plane wave $|\epsilon_f, \mathbf{k}_\parallel\rangle$ advancing onto the crystal surface. Using the standard layer-KKR method[25] generalized for the relativistic case,[22,23] we first obtain the SPLEED state $-U\Psi_f(\mathbf{r})$. The final state is then given as the time-reversed SPLEED state ($U = -i\sigma_y K$ is the relativistic time inversion). Many-body effects are included phenomenologically in the SPLEED calculation, by

using a parametrized, weakly energy-dependent and complex inner potential $V_0(E_2)=V_{0r}(E_2)+iV_{0i}(E_2)$ as usual.[18] This generalized inner potential takes into account inelastic corrections to the elastic photocurrent[29] as well as the actual (real) inner potential, which serves as a reference energy inside the solid with respect to the vacuum level.[31] Due to the finite imaginary part $iV_{0i}(E_2)$, the flux of elastically scattered electrons is continuously reduced, and thus the amplitude of the high-energy wave field $\Psi_f(\mathbf{r})$ can be neglected beyond a certain distance from the surface. The practical calculation starts with the Dirac Hamiltonian h_{LSDA} ($\hbar=m=e=1$, $c=137.036$) which one has to consider in the framework of relativistic spin DFT:[32,33]

$$h_{\mathrm{LSDA}}(\mathbf{r}) = -ic\boldsymbol{\alpha}\boldsymbol{\nabla} + \beta c^2 - c^2 + V_{\mathrm{LSDA}}(r) + \beta\boldsymbol{\sigma}\mathbf{B}_{\mathrm{LSDA}}(r). \tag{2}$$

$V_{\mathrm{LSDA}}(r)$ denotes the (effective) spin-independent potential, and $\mathbf{B}_{\mathrm{LSDA}}(r)$ is the (effective) magnetic field given by:[34]

$$V_{\mathrm{LSDA}}(r) = \frac{1}{2}[V^{\uparrow}_{\mathrm{LSDA}}(r) + V^{\downarrow}_{\mathrm{LSDA}}(r)], \tag{3}$$

$$\mathbf{B}_{\mathrm{LSDA}}(r) = \frac{1}{2}[V^{\uparrow}_{\mathrm{LSDA}}(r) - V^{\downarrow}_{\mathrm{LSDA}}(r)]\mathbf{b}. \tag{4}$$

The constant unit vector $\mathbf{b}$ determines the spatial direction of the (uniform) magnetization as well as the spin quantization axis. β denotes the usual 4×4 Dirac matrix with the nonzero diagonal elements $\beta_{11}=\beta_{22}=1$ and $\beta_{33}=\beta_{44}=-1$, and the vector $\boldsymbol{\alpha}$ is given by its components $\alpha_k=\sigma_x\otimes\sigma_k$ ($k=x,y,z$) in terms of the 2×2 Pauli-matrices σ_k. Solutions of the corresponding Dirac equation may be found by use of the phase-functional ansatz of Calogero[35] generalized to the relativistic case.[25,36,37]

The "low-energy" propagator G_1^+ in Eq. (1), i.e., the one-electron retarded Green function for the initial state in the operator representation, yields the "raw spectrum." It is directly related to the "bare" photocurrent and thereby represents the central physical quantity within the one-step model. $G_1^+\equiv G_1^+(E_i)$ is to be evaluated at the initial-state energy $E_i\equiv\epsilon_f-\omega-\mu_0$, where ω is the photon energy (μ_0 stands for the chemical potential). In the relativistic case G_1^+ is described by a 4×4 Green matrix which has to be obtained for a semi-infinite stack of layers. This quantity is defined by the following equation:

$$[E_i + \mu_0 - h_{\mathrm{LSDA}}(\mathbf{r})]G_1^+(\mathbf{r},\mathbf{r}',E_i) = -\delta(\mathbf{r}-\mathbf{r}'). \tag{5}$$

In order to account for strong electronic correlations beyond the LSDA-scheme one has to introduce a nonlocal, energy, and spin-dependent potential U. This quantity can be defined in the following way:

$$U(\mathbf{r},\mathbf{r}',E) = \delta(\mathbf{r}-\mathbf{r}')[V_{\mathrm{LSDA}}(\mathbf{r}) + \beta\boldsymbol{\sigma}\mathbf{B}_{\mathrm{LSDA}}(\mathbf{r})] + \Sigma^{(V)} \times(\mathbf{r},\mathbf{r}',E) + \beta\boldsymbol{\sigma}\boldsymbol{\Sigma}^{(\mathbf{B})}(\mathbf{r},\mathbf{r}',E), \tag{6}$$

with

$$\Sigma^{(V)}(\mathbf{r},\mathbf{r}',E) = \frac{1}{2}[\Sigma^{\uparrow}(\mathbf{r},\mathbf{r}',E) + \Sigma^{\downarrow}(\mathbf{r},\mathbf{r}',E)] \tag{7}$$

and

$$\boldsymbol{\Sigma}^{(\mathbf{B})}(\mathbf{r},\mathbf{r}',E) = \frac{1}{2}[\Sigma^{\uparrow}(\mathbf{r},\mathbf{r}',E) - \Sigma^{\downarrow}(\mathbf{r},\mathbf{r}',E)]\mathbf{b}. \tag{8}$$

The resulting integrodifferential equation for the initial-state one-electron retarded Green function takes the form:

$$[E + \mu_0 + ic\boldsymbol{\alpha}\boldsymbol{\nabla} - \beta c^2 + c^2)]G_1^+(\mathbf{r},\mathbf{r}',E) + \int U(\mathbf{r},\mathbf{r}'',E)G_1^+(\mathbf{r}'',\mathbf{r}',E)d\mathbf{r}'' = \delta(\mathbf{r}-\mathbf{r}'). \tag{9}$$

According to the LSDA+DMFT approach realized in the framework of the fully relativistic Korringa-Kohn-Rostoker multiple scattering theory (SPR-KKR)[38] we use a self-energy $\Sigma^{\mathrm{DMFT}}(E)$ calculated self-consistently using dynamical mean-field theory (DMFT).[39]

The explicit form in relativistic notation is given by:

$$U_{\Lambda\Lambda'}(\mathbf{r},\mathbf{r}',E) = [V(\mathbf{r}) + \hat{\boldsymbol{\sigma}}B(\mathbf{r})]\delta(\mathbf{r}-\mathbf{r}') + \Sigma^{\mathrm{DMFT}}_{\Lambda\Lambda'}(E)\delta_{l2}\delta_{l'2}. \tag{10}$$

The spin-orbit quantum number κ and magnetic quantum number μ were combined in the symbol $\Lambda=(\kappa,\mu)$.

B. LSDA+DMFT treatment of disordered alloys

In this section we shortly review the coherent potential approximation (CPA)[40,41] within LSDA+DMFT scheme. CPA is considered to be the best theory among the so-called single-site (local) alloy theories that assume complete random disorder and ignore short-range order. This scheme is implemented within the above mentioned SPR-KKR method. The combination of the CPA and LSDA+DMFT turned out to be a quite powerful technique to calculate electronic structure properties of substitutionally disordered correlated materials.[38,42,43] Within the CPA the configurationally averaged properties of a disordered alloy are represented by a hypothetical ordered CPA medium, which in turn may be described by a corresponding site-diagonal scattering path operator τ^{CPA}, which in turn is closely connected with the electronic Green's function. The corresponding single-site t-matrix t_c^{CPA} and multiple scattering path operator τ^{CPA} are determined by the so called CPA-condition:

$$x_{\mathrm{A}}\tau^{\mathrm{A}} + x_{\mathrm{B}}\tau^{\mathrm{B}} = \tau^{\mathrm{CPA}}. \tag{11}$$

For example a binary system $\mathrm{A}_x\mathrm{B}_{1-x}$ composed of components A and B with relative concentrations x_{A} and x_{B} is considered. The above equation represents the requirement that embedding substitutionally an atom (of type A or B) into the CPA medium should not cause additional scattering. The scattering properties of an A atom embedded in the CPA medium, are represented by the site-diagonal component-projected scattering path operator τ^{A} (angular momentum index omitted here)

$$\tau^{\mathrm{A}} = \tau^{\mathrm{CPA}}[1 + (t_{\mathrm{A}}^{-1} - t_{\mathrm{CPA}}^{-1})\tau^{\mathrm{CPA}}]^{-1}, \tag{12}$$

where t_{A} and t_{CPA} are the single-site matrices of the A component and of the CPA effective medium. A corresponding equation holds also for the B component in the CPA medium. The coupled sets of equations for τ^{CPA} and t^{CPA} have to be solved iteratively within the CPA cycle. The quantity $\mathcal{D}=[1+(t_{\mathrm{A}}^{-1}-t_{\mathrm{CPA}}^{-1})]^{-1}$ is called CPA-projector.

The above scheme can straightforwardly be extended to include the many-body correlation effects for disordered alloys.[38] According to the LSDA+DMFT approach realized in the framework of the fully relativistic SPR-KKR multiple scattering theory we use a self energy $\Sigma_A^{\mathrm{DMFT}}(E)$ calculated self-consistently using dynamical mean field theory.[39] Within the KKR approach the local multiorbital and energy dependent self-energies $[\Sigma_A^{\mathrm{DMFT}}(E)$ and $\Sigma_B^{\mathrm{DMFT}}(E)]$ are directly included into the single-site matrices t_A and t_B, respectively by solving the corresponding Dirac Eq. (9). Consequently, all the relevant physical quantities connected with the Green's function and used in the next section, as for example, the matrix elements or scattering matrices like t^{CPA} contain the electronic correlations beyond the LSDA scheme.

C. Calculation of the photocurrent

The first step in an explicit calculation of Eq. (1) consists in the setup of the relativistic SPLEED-formalism within the CPA theory. The coherent scattering matrix t_{cn}^{CPA} for the nth atomic site together with the crystal geometry determines the scattering matrix M for a certain layer of the semi-infinite half space:

$$M_{\mathbf{g}\mathbf{g}'}^{\tau\tau' ss'} = \delta_{\mathbf{g}\mathbf{g}'}^{\tau\tau' ss'} + \frac{8\pi^2}{k k_{\mathbf{g}z}^{+}} \sum_{\substack{nn' \\ \Lambda\Lambda'\Lambda''}} i^{-l} C_{\Lambda}^{m_s} Y_l^{\mu - m_s}(\hat{\mathbf{k}}_{\mathbf{g}}^{\tau}) * t_{cn}^{\mathrm{CPA}}{}_{\Lambda\Lambda''} (1-X)^{-1}_{\Lambda''\Lambda'} i^{l'} C_{\Lambda'}^{m_s'} Y_{l'}^{\mu' - m_s'}(\hat{\mathbf{k}}_{\mathbf{g}'}^{\tau'}) * e^{-i(\mathbf{k}_{\mathbf{g}}^{\tau}\mathbf{R}_n + \mathbf{k}_{\mathbf{g}'}^{\tau'}\mathbf{R}_{n'})}. \tag{13}$$

By means of the layer-doubling technique the so called bulk-reflection matrix can be calculated, which gives the scattering properties of a semi-infinite stack of layers. Finally applying the SPLEED-theory[25] we are able to derive the final state for the semi-infinite crystal.

Δ in Eq. (1) is the dipole operator in the electric dipole approximation which is well justified in the visible and ultraviolet spectral range. It mediates the coupling of the high-energy final state with the low-energy initial states. In a fully relativistic theory the dipole interaction of an electron with the electromagnetic field is given by the dipole operator $\Delta=-\boldsymbol{\alpha}\mathbf{A}_0$ where $\mathbf{A}_0$ is the spatially constant vector potential inside the crystal. Dealing with the matrix element $\langle\Psi_f|\Delta|\Psi_i\rangle$ between eigenspinors $|\Psi_f\rangle$ and $|\Psi_i\rangle$ of the Dirac Hamiltonian with energies E_f and E_i, respectively, Δ is given by:

$$\Delta = E\left(\mathbf{A}_0\boldsymbol{\nabla} + \frac{i\omega}{c}\boldsymbol{\alpha}\mathbf{A}_0\right)V_{\mathrm{LSDA}} + E(\mathbf{A}_0\boldsymbol{\nabla})\beta\boldsymbol{\sigma}\mathbf{B}_{\mathrm{LSDA}} + E\frac{\omega}{c}\beta\mathbf{A}_0\times\boldsymbol{\sigma}\mathbf{B}_{\mathrm{LSDA}}, \tag{14}$$

with $E=-2ic/[(E_f+c^2)^2-(E_i+c^2)^2]$. The expression is derived by making use of commutator and anticommutator rules analogously to the nonrelativistic case in Ref. 44.

According to Pendry[19] the calculation of G_1^+, and in consequence the calculation of the photocurrent, can be divided into four different steps. The first contribution I^{a}, the so called "atomic contribution" results from the replacement of G_1^+ in Eq. (1) by $G_{1,a}^+$. The second contribution I^{m}, describes the multiple scattering of the initial state. The third contribution I^{s} to the photocurrent takes care of the surface. When dealing with the disorder in the alloys, an additional I^{inc}, the so called "incoherent" term appears. Following Durham *et al.*[27,28] we have to perform the configurational average of these four contributions:

$$\langle I^{\mathrm{PES}}(\epsilon_f,\mathbf{k}_{\parallel})\rangle = \langle I^{\mathrm{a}}(\epsilon_f,\mathbf{k}_{\parallel})\rangle + \langle I^{\mathrm{m}}(\epsilon_f,\mathbf{k}_{\parallel})\rangle + \langle I^{\mathrm{s}}(\epsilon_f,\mathbf{k}_{\parallel})\rangle + \langle I^{\mathrm{inc}}(\epsilon_f,\mathbf{k}_{\parallel})\rangle. \tag{15}$$

For the atomic contribution the averaging procedure is trivial, since $\langle I^{\mathrm{a}}(\epsilon_f,\mathbf{k}_{\parallel})\rangle$ is a single site quantity. The atomic contribution is build up by a product between the matrix $\mathcal{Z}_{jn\alpha_n}^{\mathrm{a}}$ and the coherent multiple scattering coefficients $A_{jn\Lambda}^{c}$ of the final state. Herein n denotes the nth cell of the jth layer and Λ denotes again the combined relativistic index. It follows:

$$\langle I^{\mathrm{a}}(\epsilon_f,\mathbf{k}_{\parallel})\rangle \propto \mathrm{Im}\sum_{\substack{jn\alpha_n \\ \Lambda\Lambda'}} x_{jn\alpha_n} A_{jn\Lambda}^{c} \mathcal{Z}_{jn\alpha_n\,\Lambda\Lambda'}^{\mathrm{a}} A_{jn\Lambda'}^{c*}, \tag{16}$$

at which α_n denotes the different atomic species located at a given atomic site n of the jth layer. The corresponding concentration is given by $x_{jn\alpha_n}$.

For an explicit calculation $\mathcal{Z}^{\mathrm{a}}$ must be separated into angular matrix elements and radial double matrix elements. A detailed description of the matrix $\mathcal{Z}^{\mathrm{a}}$ and of the multiple scattering coefficients $A_{jn\Lambda}^{c}$ for the different atomic species is given in Refs. 22 and 23.

The intra(inter)-layer contributions $\langle I^{\mathrm{m}}(\epsilon_f,\mathbf{k}_{\parallel})\rangle$ to the photocurrent describe the multiple scattering corrections of the initial state G_1^+ between and within the layers of the single crystal. They can be written in a similar form:

$$\langle I^{\mathrm{m}}(\epsilon_f,\mathbf{k}_{\parallel})\rangle \propto \mathrm{Im}\sum_{\substack{jn \\ \Lambda\Lambda'}} A_{jn\Lambda}^{c} \mathcal{Z}_{jn\,\Lambda\Lambda'}^{c(2)} C_{jn\Lambda'}^{B,G}. \tag{17}$$

In analogy to the atomic contribution the coherent matrix $\mathcal{Z}^{c(2)}$ can be separated into angular and radial parts. The difference to the atomic contribution is that the radial part of the matrix $\mathcal{Z}^{c(2)}$ consists of radial single matrix elements instead of radial double integrals. In the alloy case this matrix results in the following expression:

$$\mathcal{Z}^{c(2)}_{\substack{jn \\ \Lambda\Lambda'}} = \sum_{\substack{\alpha_n \\ \Lambda_1\Lambda_2\Lambda_3}} x_{jn\alpha_n} R^{(2)}_{\substack{jn\alpha_n \\ \Lambda_1\Lambda\Lambda_2\Lambda_3}} \mathcal{D}^{jn\alpha_n}_{\Lambda_3\Lambda'} D_{\Lambda_1\Lambda_2}. \tag{18}$$

The radial and angular parts of the matrix element are denoted by $R^{(2)}$ and D. The CPA-average procedure explicitly is represented in terms of the CPA-projector $\mathcal{D}_{jn\alpha_n}$ representing the α species at site n for layer j. C^B and C^G denote the coherent multiple scattering coefficients of the initial state within a layer and between different layers. They have the form:

$$C^B_{jn\Lambda} = \sum_{n'\Lambda'\Lambda''} B^{(o)c}_{jn'\Lambda'} (t_c^{\mathrm{CPA}})^{-1}_{\substack{jn' \\ \Lambda'\Lambda''}} ((1-X)^{-1}_{\substack{jnn' \\ \Lambda''\Lambda}} - \delta^{nn'}_{\Lambda''\Lambda}), \tag{19}$$

with the coherent bare amplitudes $B^{(o)c}_{jn'\Lambda'}$:

$$B^{(o)c}_{jn'\Lambda'} = \sum_{\Lambda''} \mathcal{Z}^{c(1)}_{\substack{jn' \\ \Lambda'\Lambda''}} A^{c*}_{jn'\Lambda''}. \tag{20}$$

with

$$\mathcal{Z}^{c(1)}_{\substack{jn \\ \Lambda\Lambda'}} = \sum_{\substack{\alpha_n \\ \Lambda_1\Lambda_2\Lambda_3}} x_{jn\alpha_n} \mathcal{D}^{T}_{\substack{jn\alpha_n \\ \Lambda\Lambda_3}} R^{(1)}_{\substack{jn\alpha_n \\ \Lambda_1\Lambda_3\Lambda_2\Lambda'}} D^{*}_{\Lambda_1\Lambda_2}. \tag{21}$$

Finally, the coherent scattering coefficients C^G for the interlayer contribution take the form:

$$C^G_{jn\Lambda} = \sum_{n'\Lambda'} G^{(o)c}_{jn'\Lambda'} (1-X)^{-1}_{\substack{jn'n \\ \Lambda'\Lambda}} \tag{22}$$

and the coherent bare amplitudes $G^{(o)c}_{jn'\Lambda'}$ are given by:

$$G^{(o)c}_{jn'\Lambda'} = \sum_{\mathbf{g}m_s} 4\pi i^{l'}(-)^{\mu'-s} C^{m_s}_{\Lambda'} * (d^{+}_{j\mathbf{g}m_s} Y^{m_s-\mu'}_{l'}(\widehat{k^{+}_{1\mathbf{g}}}) e^{i\mathbf{k}^{+}_{1\mathbf{g}}\cdot\mathbf{r}_{n'}} + d^{-}_{j\mathbf{g}m_s} Y^{m_s-\mu'}_{l'}(\widehat{k^{-}_{1\mathbf{g}}}) e^{i\mathbf{k}^{-}_{1\mathbf{g}}\cdot\mathbf{r}_{n'}}). \tag{23}$$

The coefficients $d^{\pm}_{j\mathbf{g}m_s}$ in Eq. (23) represent the plane-wave expansion of the initial state between the different layers of the semi-infinite stack of layers. For a detailed description of the matrices $\mathcal{Z}^{a}$, $\mathcal{Z}^{(1)}$, and $\mathcal{Z}^{(2)}$ and of the multiple scattering coefficients $d^{\pm}_{j\mathbf{g}m_s}$ the reader again is referred to Refs. 22 and 23.

Within the contribution $\langle I^s(\epsilon_f,\mathbf{k}_\parallel)\rangle$ one takes care of the surface of the semi-infinite crystal. According to Durham[27] the surface contribution remains unchanged compared to the ordered case: $\langle I^s(\epsilon_f,\mathbf{k}_\parallel)\rangle = I^s(\epsilon_f,\mathbf{k}_\parallel)$. In particular, it follows for the surface part of the photocurrent:

$$I^s(\epsilon_f,\mathbf{k}_\parallel) \propto \mathrm{Im}\int d\mathbf{r}\Psi^{*s}_f(\mathbf{r})\Delta\Psi^s_i(\mathbf{r}), \tag{24}$$

with

$$\Psi^s_i(\mathbf{r}) = \int d\mathbf{r}' G^{+}_s(\mathbf{r},\mathbf{r}')\Delta^{*}\Psi^s_f(\mathbf{r}'). \tag{25}$$

In the case of a z-dependent barrier potential $V_B = V_B(z)$, the initial and final state wave fields have to be calculated numerically in the surface region, as it has been shown by Grass *et al.*[45] Both wave fields $\Psi^s_i(\mathbf{r})$ and $\Psi^s_f(\mathbf{r})$ can be decomposed into z dependent and corresponding parallel components

$$\Psi^s_i(\mathbf{r}) = \sum_{\mathbf{g}} \phi_{\mathbf{g}}(z) e^{i\mathbf{k}_{i\mathbf{g}\parallel}(\mathbf{r}-\mathbf{c})_\parallel}, \tag{26}$$

$$\Psi^s_f(\mathbf{r}) = \sum_{\mathbf{g}} \chi_{\mathbf{g}}(z) e^{i\mathbf{k}_{f\mathbf{g}_\parallel}(\mathbf{r}-\mathbf{c})_\parallel}, \tag{27}$$

with the regular solutions of the Schrödinger equation $\phi_{\mathbf{g}}$ and $\chi_{\mathbf{g}}$ to the reciprocal lattice vector $\mathbf{g}$ for $V_B(z)$ in the range $-\infty < z < c_z$. The value c_z defines the point, where the surface potential joins smoothly to the inner potential of the bulk crystal.

Final evaluation of the surface contribution gives:

$$I^s(\epsilon_f,\mathbf{k}_\parallel) \propto \mathrm{Im}\sum_{\mathbf{g}} e^{i\mathbf{q}_\parallel\cdot\mathbf{c}_\parallel} A_z \int_{-\infty}^{c_z} \psi_{\mathbf{g}} V'_B \chi_{\mathbf{g}} e^{iq_z z} dz, \tag{28}$$

where A_z is the z component of the amplitude $\mathbf{A}_0$ and $\mathbf{q}$ is the wave vector of the photon field. For a step barrier $V_B(z) = V_{\mathrm{or}}\Theta(z-c_{1z})$, where Θ is the unit step function, Pendry's result[19] will be reproduced. V_{or} denotes the constant inner potential of the bulk crystal.

The last contribution to the alloy photocurrent is the so called incoherent part $\langle I^{\mathrm{inc}}(\epsilon_f,\mathbf{k}_\parallel)\rangle$, which appears because the spectral function of an disordered alloy[40] is defined as a non-single-site quantity. In fact this contribution is closely connected with the presence of the irregular wave functions well known from the spherical representation of the Green function G^{+}_1. The incoherent term is defined as:

$$\langle I^{\mathrm{inc}}(\epsilon_f,\mathbf{k}_\parallel)\rangle \propto \sum_{\substack{jn\alpha_n \\ \Lambda\Lambda'\Lambda''\Lambda'''}} x_{jn\alpha_n} A^{c}_{jn\Lambda} \mathcal{Z}^{(1)}_{\substack{jn\alpha_n \\ \Lambda\Lambda'}} * (\tau^{00}_{jn\alpha_n} - t_{jn\alpha_n})_{\Lambda'\Lambda''} \mathcal{Z}^{(2)}_{\substack{jn\alpha_n \\ \Lambda''\Lambda'''}} A^{c*}_{jn\Lambda'''} + \sum_{\substack{jn \\ \Lambda\Lambda'\Lambda''\Lambda'''}} A^{c}_{jn\Lambda} \mathcal{Z}^{c(1)}_{\substack{jn \\ \Lambda\Lambda'}} \tau^{00}_{\substack{cjn \\ \Lambda'\Lambda''}} \mathcal{Z}^{c(2)}_{\substack{jn \\ \Lambda''\Lambda'''}} A^{c*}_{jn\Lambda'''}, \tag{29}$$

at which $\tau^{00}_{jn\alpha_n}$ denotes the one-site restricted average CPA matrix for species α_n at atomic site n for layer j. τ^{00}_{cjn} represents the corresponding matrix for the coherent medium. The incoherent part $\langle I^{\mathrm{inc}}(\epsilon_f,\mathbf{k}_\parallel)\rangle$ completes the CPA-averaged photocurrent within the fully relativistic one-step model. The next chapter deals with the experimental and computational details of our explicit photocurrent analysis for the ferromagnetic binary alloy Ni_xPd_{1-x}.

III. COMPUTATIONAL AND EXPERIMENTAL DETAILS

A. Computational details

The self-consistent electronic structure calculations were performed within the *ab initio* framework of spin-density-functional theory. The Vosko, Wilk, and Nusair parametriza-

tion of the exchange and correlation potential was used.[46] The electronic structure was calculated in a fully relativistic mode by solving the corresponding Dirac equation. This was achieved using the spin polarized relativistic multiple scattering or Korringa-Kohn-Rostoker formalism.[47] To account for electronic correlations beyond the LSDA[16,17] we employed a combined LSDA+DMFT scheme, self-consistent in both the self-energy calculation and in the charge density calculation, as implemented within the relativistic SPR-KKR formalism.[38] As a DMFT-solver the relativistic version of the so-called spin-polarized T-matrix plus fluctuation exchange (SPTF) approximation[48,49] was used. In contrast to most other LSDA+DMFT implementations, within the SPR-KKR scheme the complex and energy-dependent self-energy Σ_{DMFT} is implemented as an additional energy-dependent potential to the radial Dirac equation, which is solved in order to calculate the new Green's function. This procedure is repeated until self-consistency in both the self-energy and the charge density is achieved. The double counting problem (separation of the Hubbard Hamiltonian from the LSDA one) was considered within the usual around mean-field (AMF) limit. This scheme was successfully used before in describing magneto-optics,[50] photoemission,[51–53] and orbital magnetic moments[42] in 3*d* transition metals.

An appealing feature of the multiple scattering formalism is the possibility to calculate substitutionally disordered materials within the CPA. The CPA is considered to be the best theory among the so-called single-site (local) alloy theories that assume complete random disorder and ignore short-range order. A combination of the CPA and LSDA+DMFT within SPR-KKR method has been used recently.[38,42,43] The self-energy within the DMFT is parametrized by the average screened Coulomb interaction U and the Hund exchange interaction J. The J parameter can be calculated directly within the LSDA and is approximately the same for all 3*d* elements; we used $J_{\mathrm{Ni}}=0.9$ eV for the Ni atoms throughout our work. The parameter U is strongly affected by the metallic screening and it is estimated for the 3*d* metals between 1–3 eV. We used $U_{\mathrm{Ni}}=2.3$ eV for the Ni atoms. As far as it concerns the Pd atoms, the local correlation effects are often assumed to be insignificant for noble metals. However, it was shown in recent LSDA+DMFT (Ref. 43) and LSDA+U studies[54] that for CoPt alloys a nonzero U value for Pt is necessary to reproduce the experimental values for the orbital magnetic moments and for the magnetocrystalline anisotropy. Following this arguments we used $U_{\mathrm{Pd}}=0.5$ eV and $J_{\mathrm{Pd}}=0.9$ eV. DMFT calculations have been performed for $T=400$ K and we used 4096 Matsubara poles to calculate the corresponding SPTF self-energy. The effective potentials were treated within the atomic sphere approximation (ASA). As mentioned above the investigated $\mathrm{Ni}_x\mathrm{Pd}_{1-x}$ alloy films were epitaxially grown on a $\mathrm{Cu}_3\mathrm{Au}(100)$ substrate. Therefore, our calculations are based on the fcc structure with the $\mathrm{Cu}_3\mathrm{Au}$ lattice constant ($a_{lat}=3.746$ Å) fixed for all concentrations x. For the multipole expansion of the Green's function, an angular momentum cutoff of $l_{\max}=3$ was used. The integration in the $\boldsymbol{k}$ space was performed by the special points method using 1600 $\boldsymbol{k}$ points in the irreducible wedge.

For the photoemission calculations we had to use a concentration-dependent inner potential V_o, since the Fermi energy depends on the composition. Lifetime effects in the initial states have been included via the imaginary part of the complex self-energy obtained from the self-consistent LSDA+DMFT calculation. To take care of impurity scattering a small constant imaginary value of $iV_i=0.05$ eV was added to Im Σ^{DMFT} for the complete series of alloys. For the final states a constant imaginary part $iV_f=2.0$ eV has been chosen in a phenomenological way, again independent from the concentration x. A crucial point for a quantitative evaluation of our photoemission data is an appropriate adaption of the surface potential. It is known for a long time that the local density approximation, and probably gradient-corrected schemes as well, are not able to provide the correct asymptotics of a potential away from the crystal surface. Therefore, a DFT surface potential gives only a good description for surface states which are located near the Fermi energy. This is not, however, a general shortcoming of the density functional theory. It has been demonstrated, e.g., by Gunnarsson *et al.*[17,55] that in the weighted-density approximation a model function describing the shape of the exchange-correlation hole can be tuned in such a way as to fulfill several physically important limiting conditions, including the $1/z$ asymptotics of the potential outside a solid surface. The *ab initio* calculations incorporating the weighted-density approximation remain, however, relatively rare and have not yet been, to our knowledge, successfully applied to the study of surface-related states. So far, an *ad hoc* adjustment of the potential barrier near the surface remains an acceptable alternative. A realistic description of the surface potential is given through a spin-dependent Rundgren-Malmström barrier,[26] which connects the asymptotic regime $z<z_A$ to the bulk muffin-tin zero V_{or} by a third order polynomial in z, spanning the range $z_A<z<z_E$. In other words z_E defines the point where the surface region end and the bulk region starts, at which z_I defines the position of the classical image plane. The values of the three parameters z_I, z_A and z_E, which finally lead to a quantitative agreement between the measured and the calculated spectra are the following: $z_I^{\uparrow(\downarrow)}=-1.80(-1.80)$ a.u., $z_A^{\uparrow(\downarrow)}=-3.36(-3.36)$ a.u. and $z_E^{\uparrow(\downarrow)}=0.0(0.0)$ a.u.. This parametrization was chosen as concentration independent and has been optimized by comparison with the experimental data. For details of the procedure the reader is referred to Ref. 22. Nevertheless, the surface potential itself depends on the concentration because the inner potential is concentration dependent due to the change of the Fermi level with x. In consequence one should expect energetic shifts of surface features as a function of the concentrations x. The calculated intensity distributions have been multiplied with the Fermi function and convoluted with a Gaussian of FWHM=0.3 eV to account for the finite resolution of the experiment.

B. Experimental details

The preparation of the $\mathrm{Ni}_x\mathrm{Pd}_{1-x}$ films and the photoemission experiments have been performed under ultra-high-vacuum conditions (base pressure $<2\cdot10^{-10}$ mbar). For this purpose, we connected a preparation chamber housing all necessary devices to grow and characterize our samples with

a second chamber especially dedicated to perform photoemission spectroscopy. In this chamber we combined two spectrometer systems, a SES 100, a hemispherical electron analyzer [manufacturer: VGScienta, Sweden], and a cylindrical sector analyzer CSA 300 [manufacturer: Focus GmbH, Germany] equipped with a low-energy electron spin-polarization detector. The experiments were conducted at the undulator beamline U125–1-PGM at the BESSY synchrotron radiation facility in Berlin. The 15 monolayer thick alloy films were grown *in situ* on a $Cu_3Au(100)$ crystal that was repeatedly sputtered with Ar ions and annealed until a clean and flat surface could be verified by Auger electron spectroscopy (AES) and low-energy electron diffraction (LEED). Nickel (purity 99.999%) and Palladium (purity 99,95%) were simultaneously co-evaporated by electron beam assisted heating of two separate rod materials allowing one to prepare films with any desired alloy composition. The thickness of the alloy films was precisely monitored by the intensity oscillation of a diffracted electron beam (kinetic energy 2 keV) during film growth. This technique called medium energy electron diffraction (MEED) displays a periodic oscillation of the (0,0) beam provided that the films grows in a layer-by-layer mode (Frank—van der Merwe growth). Our MEED data showed a pronounced intensity oscillation for the $Ni_{0.33}Pd_{0.67}$ film. This observation matches nicely with the vanishing lattice misfit for $Ni_{0.36}Pd_{0.64}$, assuming a linear dependency between alloy composition and lattice misfit. For $Ni_{0.47}Pd_{0.53}$ we found less pronounced intensity oscillations over the complete thickness range, while $Ni_{0.67}Pd_{0.33}$ exhibited only even weaker oscillations that were fading away at ~11 ML. From these observations we can deduce an almost perfect surface quality for $Ni_{0.33}Pd_{0.67}$ that deteriorates for $Ni_{0.47}Pd_{0.53}$, and even more for $Ni_{0.67}Pd_{0.33}$. The compositions of the alloy films were derived from AES studies. As mentioned above, Ni_xPd_{1-x} films may exhibit a spin-reorientation transition. In our case, due to the chosen thickness of 15 ML, the alloy films are magnetized out-of-plane independent from the alloy composition. The undulator beamline at BESSY offered linearly polarized light having the *E*-vector oriented in-plane with the incoming light and the wave vector of the detected photoelectrons. The sample was illuminated under 45° to the sample normal, while the photoelectrons emitted along the surface normal were analyzed. According to nonrelativistic dipole selection rules, only photoelectrons from initial bands with Δ_1 and Δ_5 symmetry can be excited in this geometry. The spin-integrated spectra were recorded with the SES 100 at room temperature. The energy resolution set in the beam line amounted to 70 meV, which is slightly higher than the energy resolution defined by the SES 100 settings (50 meV). The angular and energy resolved spectra were averaged within a 1 degree interval that was symmetrically centered around the normal emission direction. Each displayed spectrum is normalized to its maximum intensity value.

IV. DISCUSSION

A. Electronic structure calculations

In Fig. 1, we show element-resolved spin and orbital magnetic moments for Ni_xPd_{1-x} as calculated by the LSDA and

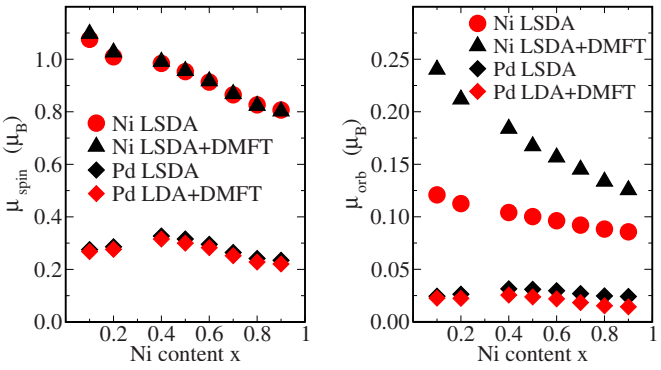

FIG. 1. (Color online) Spin (left panel) and orbital (right panel) magnetic moments of Ni_xPd_{1-x} as a function of the concentration x calculated within LSDA and LSDA+DMFT, respectively. (DMFT parameters: U_{Ni}=2.3 eV, U_{Pd}=0.5 eV, and $J_{Ni,Pd}$=0.9 eV)

the LSDA+DMFT approach. As can be seen in Fig. 1, Ni induces an appreciable spin magnetic moment on the Pd-site (about $\mu_{Pd} \approx 0.3\mu_B$) throughout the whole concentration range. The calculated average magnetic moments in Ni_xPd_{1-x} alloys agree well with the corresponding experimental ones[56] and recently calculated[57] values. However, one has to stress that our calculations presented here have been performed using the Cu_3Au lattice constant, which lies midway between Ni and Pd. Due to this fact our averaged magnetic moments are higher for the Pd- and Ni-rich alloys then corresponding experimental data measured for fcc-Ni_xPd_{1-x} alloys.[56] Using the LSDA+DMFT we obtain only slight changes of the spin magnetic moments in comparison to the LSDA calculations. While the spin magnetic moments for 3*d*-transition metals and their alloys are described rather accurately by the LSDA, the orbital magnetic moments are systematically underestimated. On the other hand, the explicit account for local many-body correlations within the LSDA+DMFT approach can improve the description of the orbital magnetic moments.[42,43] Also for Ni_xPd_{1-x} the use of the DMFT introduced remarkable change for the orbital moments as can be seen in Fig. 1. For the Ni-rich region we see a slight increase of the Pd orbital magnetic moment. In the case of Ni we obtain an increase of the orbital magnetic moment mostly by factor of two in the Pd-rich region.

In Figs. 2 and 3, we present the density of states (DOS) and spectral function calculations both as functions of the concentration x. They already allow us to qualitatively assign some spectral intensities in our photoemission data to Ni or Pd. In Fig. 3 the bare Bloch spectral functions are shown that result from a pure LSDA calculation. In addition we present the corresponding data obtained self-consistently using the LSDA+DMFT method. The element- and spin-resolved DOS's for the series of alloys (Fig. 2) range from pure Pd to pure Ni in steps of 10%, respectively, 20% of the concentration x. The paramagnetic DOS for Pd with the 4*d*-states located roughly between E_F and 3 eV binding energy and the *sp*-states at higher binding energies appear more or less unstructured, as expected. Increasing the concentration of Ni the alloys DOS gets spin split reflecting ferromagnetic order and an increasing weight of Ni 3*d*-states near the Fermi level can be observed. Moreover at about 6 eV binding energy the

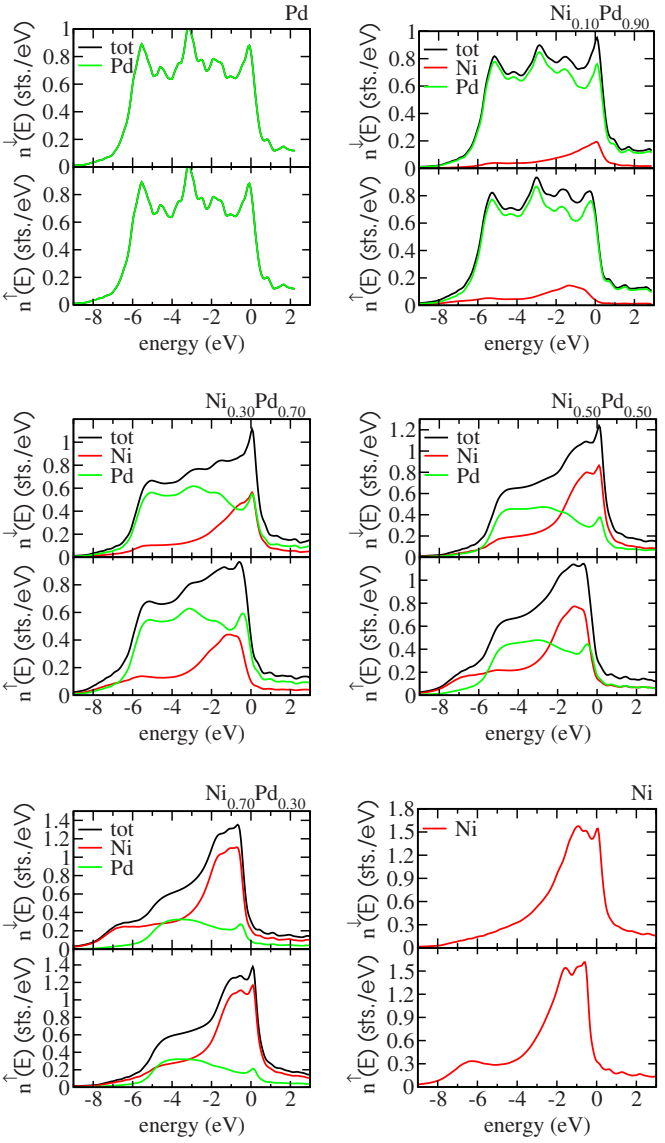

FIG. 2. (Color online) Spin- and element-resolved Ni_xPd_{1-x} DOS's as a function of the concentration x calculated within LSDA+DMFT. Upper panel left side shows the paramagnetic Pd DOS. Lower panel right side shows the ferromagnetic Ni DOS. (DMFT parameters: U_{Ni}=2.3 eV, U_{Pd}=0.5 eV, and $J_{Ni,Pd}$ =0.9 eV)

Ni *sp*-states appear. Starting with 30% of Ni the corresponding DOS's tend to be more structured with a significant shift of electronic density toward E_F. For $Ni_{0.50}Pd_{0.50}$ the strongest mixture of Ni- and Pd-states over the whole range of binding energies is observed. Due to the specific DOS distribution for pure Ni and pure Pd, we can identify a slight dominance of the Ni DOS near E_F and of the Ni 6 eV satellite for higher binding energies. Due to the perturbative nature of the SPTF solver we find the satellite at slightly higher binding energy of about 7 eV.[38] At concentrations $\geq$70% of Ni the DOS's exhibit mostly the characteristic features of the pure ferromagnetic Ni DOS. The shoulder at the Fermi level becomes more pronounced, and the dips indicating Pd states are smeared out.

More detailed information about the electronic structure is obtained from the Bloch spectral functions shown in Fig. 3. Again, the spectral functions are shown for a series of alloys, at which the concentration x varies in steps of 10%, respectively, 20% starting from pure Pd. In contrast to the LSDA+DMFT based DOS calculations shown in Fig. 2 we present LSDA as well as LSDA+DMFT based spectral functions to demonstrate the effect of strong electronic correlations in the different alloys. For the Pd-rich end of the system it is clearly observable, that due to the alloying, even for a Ni concentration of 10% the electronic states appear to be smeared out and the dispersion is reduced in general. For Ni concentrations between 30% and 70% one enters the concentration, where the smearing of electronic spectral function reaches a maximum value and the dispersion nearly vanishes over a wide range of binding energies. As it has been discussed above, this result is in fully agreement with the DOS calculations, which show the most pronounced mixing of Ni- and Pd-states within this concentration regime.

Due to the simultaneous occurrence of spin-orbit coupling and exchange splitting which is treated on equal footing in a fully relativistic theory, majority, and minority spin bands occur together for regions where the spin character is no longer well-defined due to hybridization. For that reason we refrain from explicitly distinguishing between majority and minority spin states as is done in nonrelativistic spectral function calculations.

In Fig. 3, the effect of strong electronic correlations in the electronic alloy states is visualized. The deviations between the LSDA and LSDA+DMFT based spectral functions are clearly observable. The bands resulting from the LSDA-DMFT calculation are shifted toward the Fermi level compared with the pure LSDA-derived bands. Also the dispersion behavior is different and the spin-splitting is significantly reduced. All of these effects have to be assigned to the real part of the self-energy Σ_{DMFT} that acts as a nonlocal, spin-, and energy-dependent potential on the various *d*-bands of Ni and Pd. Furthermore the smearing of the different bands resulting from the alloying effect is enhanced due to the imaginary part of the self-energy Σ_{DMFT}, which is energy-dependent too. These effects, of course, should be observable in the corresponding photoemission spectra that will be discussed in the next subsection.

B. One-step calculations

Concerning the spectroscopic analysis we restrict ourselves to the range of concentrations where the alloying effect is most pronounced. This is, as discussed before, the case for $Ni_{0.30}Pd_{0.70}$, $Ni_{0.50}Pd_{0.50}$, and $Ni_{0.70}Pd_{0.30}$ alloys. In Fig. 4, we present a series of normal emission ARUPS spectra for photon energies ranging from 18 to 40 eV. The angle of light incidence was chosen 45° to the surface normal and the linear polarization was directed horizontal to the reaction plane. In the left panel we show the theoretical photoemission spectra for $Ni_{0.30}Pd_{0.70}$ that are based on a pure LSDA-like electronic structure calculation. The measured spectra are shown in the middle panel. For reasons of comparison and to demonstrate the effect of strong electronic correlations

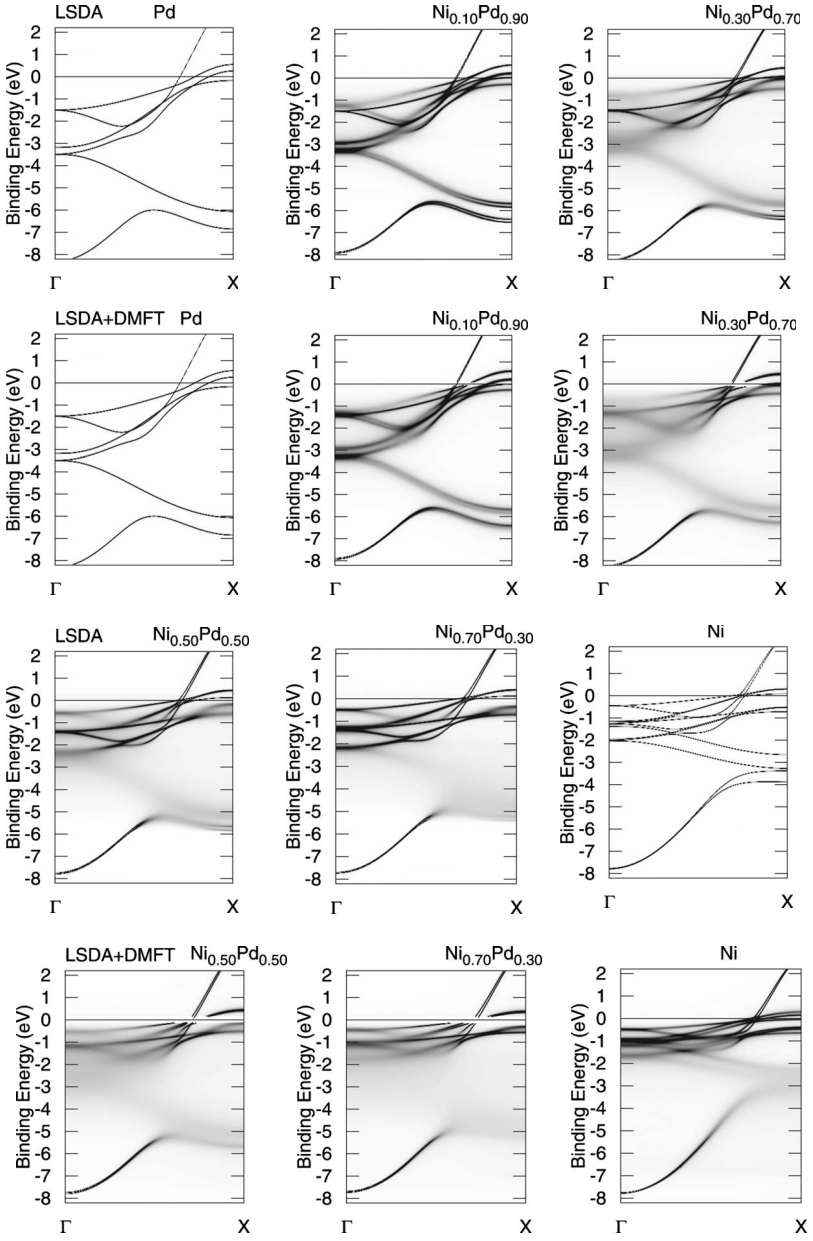

FIG. 3. Spin-polarized Ni_xPd_{1-x} bare Bloch spectral functions for different concentrations x. We show the LSDA (first and third row) and LSDA+DMFT (second and fourth row) based calculations starting from pure Pd (upper panel, left side) to pure Ni (lower panel, right side)

we additionally present the theoretical LSDA+DMFT based spectra in the right panel of Fig. 4.

As most prominent feature we observe a dominant peak that disperses from 1 eV binding energy to about 2.5 eV as a function of the photon energy. This feature is, by comparison with the corresponding spectral function calculation, attributed to *d*-states which result from a strong admixture of Ni 3*d* states to the Pd 4*d* bands. The variety of different *d*-states that appear between E_F and 3 eV binding energy may be also responsible for the pronounced asymmetric line shape which even changes into a double peak structure for certain excitation energies. In the experimental data the double peak structure is much more pronounced and visible over the whole range of photon energies. We also observe a pronounced shift of spectral weight toward the Fermi level, when compared to the LSDA calculations. This shift is connected with a band narrowing indicating therefore a less pronounced dispersion compared to the LSDA prediction. Furthermore, the lifetime of the deeper lying *sp*-states is underestimated in the spectroscopic analysis. The structure calculated at about 3.5 eV binding energy is hidden in experiment on the background and the *sp*-like structure at 6 eV binding energy shows a lower intensity.

A detailed theoretical analysis within the one-step model in combination with a correlation corrected electronic structure results in the series of spectra presented in the right panel. As an expected result the dispersion behavior is reduced and the peaks are shifted toward the Fermi level. This is in much better agreement with the experiment than the LSDA based calculations. Also the relative intensities, which we obtained for the different spectra reflect quantitatively the experimental findings. Last but not least the double-peak structure is reproduced in better agreement with the experimental data, especially for higher excitation energies. A careful analysis of this two-peak feature reveals that a strong amount of surface emission takes place in the peak at lower

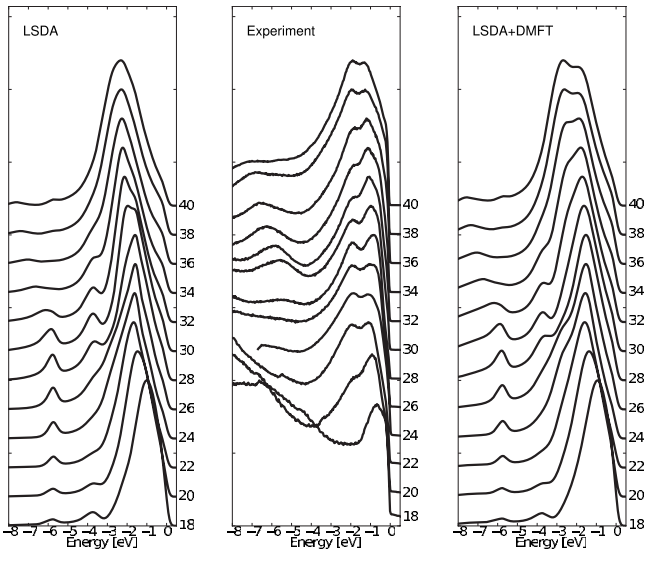

FIG. 4. ARUPS spectra of the $Ni_{0.30}Pd_{0.70}(001)$ alloy surface for different photon energies in the range from $h\nu$=18 eV to $h\nu$ =40 eV along ΓX in normal emission. The left panel presents calculated photoemission spectra based on a LSDA electronic structure calculation. The experimental spectra are presented in the middle panel and the theoretical LSDA+DMFT based spectra are shown in the right panel. Due to the high concentration of Pd the spectral distribution is more pronounced for higher binding energies.

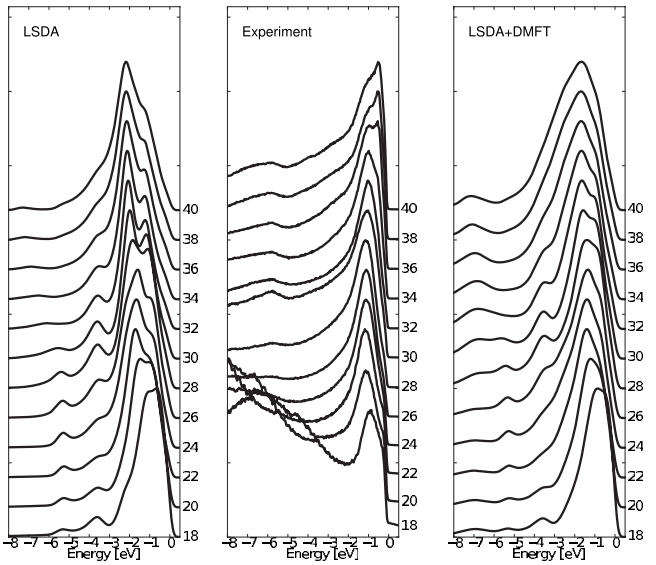

FIG. 5. Same as Fig. 4 but spectra measured and calculated for the $Ni_{0.50}Pd_{0.50}$ alloy system. As expected, Ni- and Pd-generated peak structures are visible with an intermediate energy range between 2 and 4 eV binding energy.

binding energy indicating a *d*-like surface resonance. This is because the latter one is only slightly affected when increasing the z component of the vector potential A_z. A surface state would be more sensitive to variations in A_z.

Despite the much better agreement between experiment and LSDA+DMFT based spectra we find from Fig. 4 that still some discrepancies exist. First the *sp*-like intensity distributions at higher binding energies are still overestimated in intensity. The explanation is found in the imaginary part of the electronic self-energy Σ^{DMFT} which only acts on the lifetime of the *d*-states. Adding a heuristic energy-dependent self-energy explicitly for *sp*-states would solve this problem. This was not done here to demonstrate exclusively the impact of DMFT-like corrections in the electronic states of Ni_xPd_{1-x} alloys. Furthermore, the change in the intensity ratio between the surface resonance and the bulk feature is underestimated in the theoretical analysis. The final discrepancy observed consists in the trend that the mainly Pd-associated peaks are slightly shifted to higher binding energies in the calculations, even when applying the LSDA +DMFT scheme. This is well known from other paramagnetic metals like Ag and can be explained in terms of static correlations in the Pd-states not explicitly considered here.

In Fig. 5, we present the spectroscopic quantities of the $Ni_{0.50}Pd_{0.50}$ alloy. In this case we have the most pronounced alloying effect. Over nearly the whole range of binding energies a strong mixture of all Ni- and Pd-states takes place. This is documented in the corresponding spectral function and DOS calculation as well. The experimental data show a dominant spectral feature at about 1 eV binding energy that only slightly disperses with the excitation energy. The double-peak feature is less pronounced. This observation can be explained by an increased amount of surface emission in comparison to the $Ni_{0.30}Pd_{0.70}$ alloy. Or, in other words, the alloy behaves more Ni-like for lower binding energies. Also the relative intensity distribution of the sp-states is reduced and visible only as a dip on top of a huge background. This scenario is very roughly reproduced by the LSDA-based calculation seen in the left panel of Fig. 5. The calculation results in a more broadened two-peak structure which, in contradiction to the experimental findings, shows the second peak at higher binding energy with the maximum intensity and in consequence leads to a spectral distribution that is shifted in energy by nearly 1 eV off the Fermi level.

The LSDA+DMFT calculation significantly improves the situation. The maximum in intensity is now located more or less at the experimental value, the dispersion is reduced and the two-peak features are less pronounced for all photon energies. These effects can be attributed to the electronic correlations which are better described by the LSDA+DMFT calculation. On the other hand, the calculated spectral features are still too broad. Again, the reason for this observation can be found in the Pd d-bands that should appear closer to E_F. In addition, our one-step photoemission analysis reveals that the direct Pd d-f-transitions seem to be overestimated in intensity in comparison to the corresponding Ni-type matrix elements. An explanation may be found in terms of the final states, which in general are insufficiently described even by a LSDA+DMFT calculation. With the assumption of a smaller Pd d-f-cross section a more quantitative agreement would be achieved.

The last example deals with the $Ni_{0.70}Pd_{0.30}$ alloy (see Fig. 6). Here, the agreement between experiment and theory is very satisfying. This is clearly observable when comparing the LSDA+DMFT results with the measurements presented in Fig. 6. On the other hand, the pure LSDA-based spectra shown in the left panel agree only qualitatively with the experimental data as observed for the other alloys. Therefore,

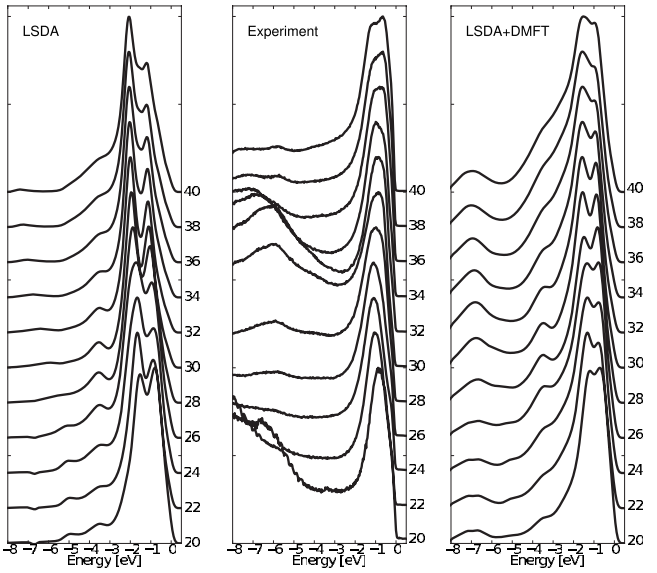

FIG. 6. Same as Fig. 4 but spectra measured and calculated for the $Ni_{0.70}Pd_{0.30}$ alloy system. Due to the high concentration of Ni the spectral distributions show the highest intensities for energies near Fermi level.

they will not be discussed in more detail here. Nevertheless, some questions are connected to the origin of the spectral distributions need to be discussed in more detail. The main peak structure at about 1 eV binding energy is dominated by Ni *d*-states. The peak at lowest binding energy is surfacelike in analogy to the pure Ni(001) surface.[58] The shoulder at about 2.5–3.0 eV binding energy is mostly due to Pd *d*-state excitations and the structure dispersing around 6.5 eV binding energy is identified as being due to excitations from the *sp*-band consisting of both Ni- and Pd-states. These findings are in line with our DOS calculations from which the distribution of Ni- and Pd-states as a function of the binding energy can be discerned. To summarize, we can state that besides the quantitative agreement only the double-peak structure shows up a bit more pronounced in theory. Furthermore, it turns out that the overall agreement for the complete alloy series is more or less quantitative when applying the LSDA+DMFT formalism, but the degree of agreement depends to some extent on the concentration. The main differences are caused by the Pd *d*-states that seem to be slightly shifted by the calculations to higher binding energies. In Figs. 4–6, we have analyzed our spectroscopic results for three different alloys to map the E versus $k_\perp$ dispersion as a function of alloying and electronic correlation in the Ni_xPd_{1-x} system. In a final step we want to study now in more detail the alloying effect by keeping the photon energy constant at $h\nu=40$ eV. Figure 7 shows a series of spectra as a function of the concentration x. The experimental data have been presented in the top panel of Fig. 7 and the corresponding LSDA+DMFT-based spectroscopic calculations are presented in the bottom panel.

Our theoretical analysis undoubtedly shows that starting from the pure Ni case, the agreement is fully quantitative within less than 0.1 eV binding energy, as expected. Going to the $Ni_{0.80}Pd_{0.20}$ alloy the agreement is on the same level of

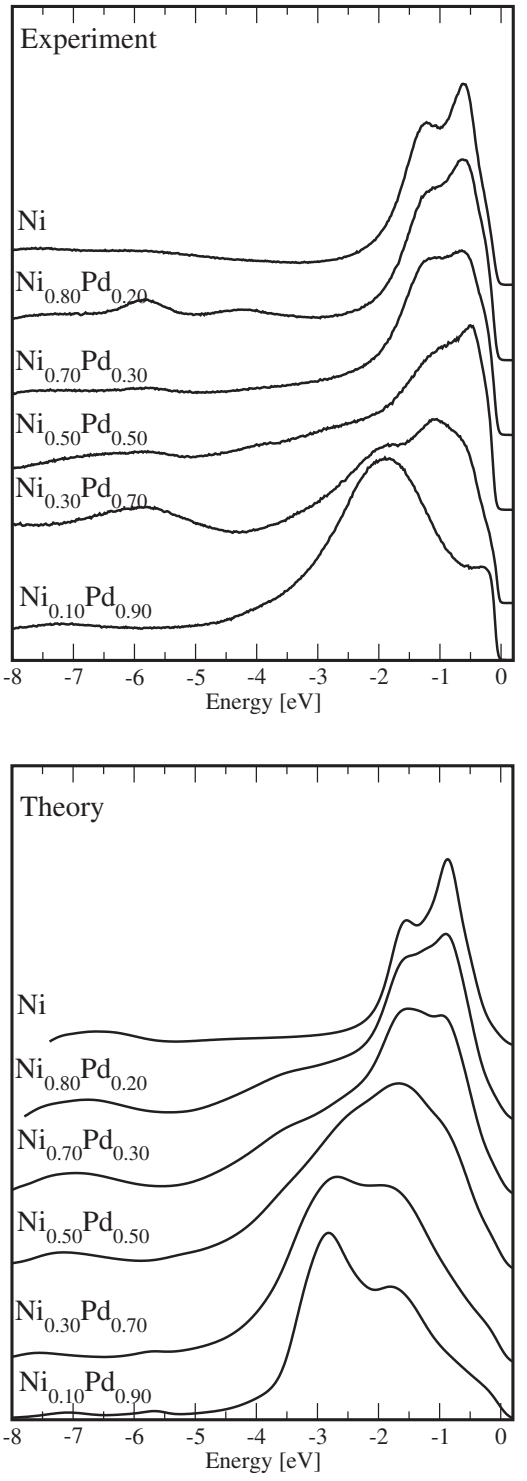

FIG. 7. ARUPS spectra taken from the $Ni_xPd_{1-x}(001)$ alloy surfaces as a function of the concentration x for a fixed photon energy of $h\nu=40.0$ eV along ΓX in normal emission. Experimental data shown at the top panel calculated spectra presented below. Depending on the concentration x a pronounced shift in spectral weight toward the Fermi level is visible.

accuracy concerning the range of binding energies between E_F and 2 eV. Inspecting the $Ni_{0.80}Pd_{0.20}$ alloy DOS this fact becomes explainable, because this energy interval represents the Ni-dominated region. The Pd-states start to appear at

about 2 eV below E_F besides of the small dip at the Fermi level. For higher binding energies the agreement is also very good, at which a bit more structure is observable in the theory, especially around 3.5 eV. An explanation for this behavior can be found in terms of lifetime effects, but it should be mentioned here that the experimental intensity background consisting of secondary electrons was not considered in the theoretical analysis on purpose. The $Ni_{0.70}Pd_{0.30}$ alloy system has been investigated extensively before and needs not to be discussed again, but as part of the concentration-dependent series it becomes much better visible that the amount of spectroscopic disagreement is mainly introduced by the increasing concentration of Pd. The same argument holds for the $Ni_{0.50}Pd_{0.50}$ and $Ni_{0.30}Pd_{0.70}$ alloys shown next in the series. In addition, the spectra of $Ni_{0.30}Pd_{0.70}$ reveal deviation near the Fermi level. The spectral intensity of the Ni surface resonance in the calculation is underestimated compared to the measurement.

We stated already in the introduction that the Ni_xPd_{1-x} alloy system poses two complications. One is an oscillatory surface segregation profile that has been deduced from LEED measurements for the $Ni_{0.50}Pd_{0.50}$ system[13] and also theoretically predicted for different crystal orientations.[59] Both theory and experiment have in common an alternating Pd enrichment and depletion as a function of the layer number. Obviously, the segregation may have a strong impact on the Ni surface resonance state located at the Fermi level. But on the basis of our experimental data we cannot qualify the segregation effect and answer the question, whether or not the discrepancy in the spectral intensity between experiment and theory may emerge due to segregation effects. It is known that the spectral height and width of surface states or resonances are modified by surface roughness. The pronounced intensity oscillations recorded by MEED during growth of the $Ni_{0.30}Pd_{0.70}$ sample indicate a smooth layer-by-layer growth and can be attributed to the perfect lattice matching between substrate and Ni_xPd_{1-x} film for this alloy concentration. As the MEED oscillations deteriorate for all other alloy concentrations we can deduce for them also an increasing smearing out of the surface resonance peak. But, although we can state a minimum for the surface roughness of the $Ni_{0.30}Pd_{0.70}$ sample, we cannot qualify this property and its influence on the spectral weight of the Ni surface resonance. Our one-step photoemission model does not take into account the surface roughness.

The last alloy concentration presented here is $Ni_{0.10}Pd_{0.90}$. Inspecting the DOS calculation one can see that the Pd contribution on the electronic structure distinguishes itself only marginally from the pure Pd metal case. Therefore, the spectral distribution shown in Fig. 7 is representative for Pd, too. A shift of spectral weight is observed when comparing experiment and theory. This is due to the combined effect of static correlations in Pd, underestimated in the calculation, and due to an overestimation of spectral weight around 3 eV binding energy. The latter one is most probably related to an insufficient description of the final states. This results in matrix elements between the Pd *d*-states and *f*-like final states that overestimate the corresponding transitions.

V. SUMMARY

Our spectroscopic analysis has clearly demonstrated that the electronic properties of the Ni_xPd_{1-x} alloy system very sensitively depend on the interplay of alloying and electronic correlation. A description within the LSDA approach in combination with a CPA method results in a qualitative description of the electronic structure of Ni_xPd_{1-x} only. The use of the CPA alloy theory self-consistently combined with a DMFT+LSDA electronic structure calculation is essential, whereas the application of the fully relativistic one-step model of photoemission, which takes into account chemical disorder and electronic correlation on equal footing guarantees a quantitative analysis of the spectroscopic data.

In our study on the ferromagnetic Ni_xPd_{1-x} alloy system we observed a complex interplay of alloying effects and electronic correlations. We found, that in order to arrive at a quantitative description of the spectroscopic measurements, it is inevitable to apply in the electronic structure calculation the CPA alloy theory self-consistently combined with the DMFT+LSDA method. Within the framework of the generalized version of the fully relativistic one-step model of photoemission, which takes into account chemical disorder and electronic correlations on equal footing we were able to model nearly all experimentally observed features in a quantitative sense. In particular, we found from our investigations that surface emission manifests itself in the double-peak structure observed for lower binding energies in a variety of photoemission spectra. A shift of spectral weight concerning the Pd states was observed from the calculations, and could be explained by an insufficient description of the Pd final-state bands in combination with an underestimation of lifetime effects in the *sp*-like states of Ni and Pd. Furthermore, the role of alloying could be disentangled from the correlation effects by a variation of the concentration x. To conclude, we were able to describe the electronic and magnetic structure of Ni_xPd_{1-x} in detail by applying a combined experimental and theoretical angle-resolved photoemission analysis. Future experimental work could probably deal with spin-resolved data in order to learn even more about the interplay of alloying, electronic correlations and relativistic effects in binary ferromagnetic alloys like Ni_xPd_{1-x}.

ACKNOWLEDGMENTS

Financial support from the Deutsche Forschungsgemeinschaft (Project Nos. EBE-154/18, MI-1327/1, and Schn-353/10) and the Bundesminsisterium für Bildung und Forschung (Grant No. 05 SC8BDA 2) is gratefully acknowledged. Thanks are due to the BESSY staff for support during the beamtime.

[1] *Magnetic Properties of Metals*, edited by H. P. J. Wijn (Springer-Verlag, Berlin, 1991).

[2] K. H. J. Buschow, in *Handbook of Magnetic Materials*, edited by K. H. J. Buschow (North Holland, Amsterdam, 1988), Vol. 4, p. 493.

[3] P. M. Oppeneer, in *Handbook of Magnetic Materials*, edited by K. H. J. Buschow (North Holland, Amsterdam, 2001), Vol. 13, p. 229.

[4] J. J. M. Franse and R. J. Radwanski, in *Handbook of Magnetic Materials*, edited by K. H. J. Buschow (North Holland, Amsterdam, 1993), Vol. 7, p. 307.

[5] T. B. Massalski, *Binary Alloy Phase Diagrams*, 2 ed. (ASM Int, Materials Park, OH, 1990).

[6] W. A. Ferrando and R. Segnan, J. Appl. Phys. **41**, 1236 (1970).

[7] M. Seider, R. Kaltofen, U. Muschiol, M.-T. Lin, and C. M. Schneider, J. Appl. Phys. **87**, 5762 (2000).

[8] F. Matthes, M. Seider, and C. M. Schneider, J. Appl. Phys. **91**, 8144 (2002).

[9] B. Schulz and K. Baberschke, Phys. Rev. **50**, 13467 (1994).

[10] A. Braun, B. Feldmann, and M. Wuttig, J. Magn. Magn. Mater. **171**, 16 (1997).

[11] W. Kuch, A. Dittschar, K. Meinel, M. Zharnikov, C. M. Schneider, J. Kirschner, J. Henk, and R. Feder, Phys. Rev. B **53**, 11621 (1996).

[12] B. Schmiedeskamp, B. Kessler, N. Müller, G. Schönhense, and U. Heinzmann, Solid State Commun. **65**, 665 (1988).

[13] G. N. Derry, C. B. McVey, and P. J. Rous, Surf. Sci. **326**, 59 (1995).

[14] *Photoemission and the Electronic Properties of Surfaces*, edited by B. Feuerbacher, B. Fitton, and R. F. Willis (Wiley, New York, 1978); *Photoemission in Solids*, edited by M. Cardona and L. Ley (Springer, Berlin, 1978), Vol. 1; J. E. Inglesfield, Rep. Prog. Phys. **45**, 223 (1982); R. Courths and S. Hüfner, Phys. Rep. **112**, 53 (1984); *Angle-Resolved Photoemission, Theory and Current Applications*, edited by S. D. Kevan, Studies in Surface Science and Catalysis Vol. 74 (Elsevier, Amsterdam, 1992).

[15] V. Dose, Prog. Surf. Sci. **13**, 225 (1983); Surf. Sci. Rep. **5**, 337 (1985); G. Borstel and G. Thörner, *ibid.* **8**, 1 (1988); N. V. Smith, Rep. Prog. Phys. **51**, 1227 (1988); M. Donath, Surf. Sci. Rep. **20**, 251 (1994).

[16] P. Hohenberg and W. Kohn, Phys. Rev. **136**, B864 (1964); W. Kohn and L. J. Sham, *ibid.* **140**, A1133 (1965); L. J. Sham and W. Kohn, *ibid.* **145**, 561 (1966).

[17] R. O. Jones and O. Gunnarsson, Rev. Mod. Phys. **61**, 689 (1989).

[18] J. B. Pendry, *Low Energy Electron Diffraction* (Academic, London, 1974).

[19] J. B. Pendry, Surf. Sci. **57**, 679 (1976).

[20] J. F. L. Hopkinson, J. B. Pendry, and D. J. Titterington, Comput. Phys. Commun. **19**, 69 (1980).

[21] G. Thörner and G. Borstel, Phys. Status Solidi B **126**, 617 (1984); J. Braun, G. Thörner, and G. Borstel, *ibid.* **130**, 643 (1985); **144**, 609 (1987); S. V. Halilov, E. Tamura, H. Gollisch, D. Meinert, and R. Feder, J. Phys.: Condens. Matter **5**, 3859 (1993); J. Henk, S. V. Halilov, T. Scheunemann, and R. Feder, Phys. Rev. B **50**, 8130 (1994); M. Fluchtmann, M. Graß, J. Braun, and G. Borstel, *ibid.* **52**, 9564 (1995).

[22] J. Braun, Rep. Prog. Phys. **59**, 1267 (1996).

[23] J. Braun, in *Band-Ferromagnetism: Ground-State and Finite-Temperature Phenomena*, edited by K. Baberschke, M. Donath, and W. Nolting (Springer, New York, 2001), p. 267.

[24] C. N. Berglund and W. E. Spicer, Phys. Rev. **136**, A1030 (1964).

[25] J. Korringa, Physica **13**, 392 (1947); W. Kohn and N. Rostocker, Phys. Rev. **94**, 1111 (1954); K. Kambe, Z. Naturforsch. **22a**, 322 (1967); A. R. Williams and J. van Morgan, J. Phys. C **7**, 37 (1974); R. G. Brown and M. Ciftan, Phys. Rev. B **27**, 4564 (1983); X.-G. Zhang, A. Gonis, and J. M. MacLaren, *ibid.* **40**, 3694 (1989); W. H. Butler and R. K. Nesbet, *ibid.* **42**, 1518 (1990); H. Ebert and B. L. Gyorffy, J. Phys. F: Met. Phys. **18**, 451 (1988); S. C. Lovatt, B. L. Gyorffy, and G. Y. Guo, J. Phys.: Condens. Matter **5**, 8005 (1993); R. Feder, J. Phys. C **14**, 2049 (1981).

[26] G. Malmström and J. Rundgren, Comput. Phys. Commun. **19**, 263 (1980).

[27] P. J. Durham, J. Phys. F: Met. Phys. **11**, 2475 (1981).

[28] B. Ginatempo, P. J. Durham, and B. I. Gyorffy, J. Phys.: Condens. Matter **1**, 6483 (1989).

[29] G. Borstel, Appl. Phys. A: Mater. Sci. Process. **38**, 193 (1985).

[30] C. Caroli, D. Lederer-Rozenblatt, B. Roulet, and D. Saint-James, Phys. Rev. B **8**, 4552 (1973).

[31] G. Hilgers, M. Potthoff, N. Müller, U. Heinzmann, L. Haunert, J. Braun, and G. Borstel, Phys. Rev. B **52**, 14859 (1995).

[32] A. K. Rajagopal and J. Callaway, Phys. Rev. B **7**, 1912 (1973).

[33] M. V. Ramana and A. K. Rajagopal, Adv. Chem. Phys. **54**, 231 (1983).

[34] P. Strange, H. Ebert, and B. L. Gyorffy, J. Phys.: Condens. Matter **1**, 2959 (1989).

[35] F. Calogero, *Variable Phase Approach to Potential Scattering* (Academic, New York, 1967).

[36] A. Gonis, *Green Functions for Ordered and Disordered Systems, Studies in Mathematical Physics 4* (North Holland, Amsterdam, 1992).

[37] X. Wang, X. G. Zhang, W. H. Butler, G. M. Stocks, and B. N. Harmon, Phys. Rev. B **46**, 9352 (1992).

[38] J. Minár, L. Chioncel, A. Perlov, H. Ebert, M. I. Katsnelson, and A. I. Lichtenstein, Phys. Rev. B **72**, 045125 (2005).

[39] G. Kotliar and D. Vollhardt, Phys. Today **57**(3), 53 (2004); A. Georges, G. Kotliar, W. Krauth, and M. J. Rozenberg, Rev. Mod. Phys. **68**, 13 (1996).

[40] J. S. Faulkner and G. M. Stocks, Phys. Rev. B **21**, 3222 (1980).

[41] P. Soven, Phys. Rev. **156**, 809 (1967).

[42] S. Chadov, J. Minár, M. I. Katsnelson, H. Ebert, D. Ködderitzsch, and A. I. Lichtenstein, EPL **82**, 37001 (2008).

[43] O. Sipr, J. Minar, S. Mankovsky, and H. Ebert, Phys. Rev. B **78**, 144403 (2008).

[44] M. Potthoff, J. Lachnitt, W. Nolting, and J. Braun, Phys. Status Solidi B **203**, 441 (1997).

[45] M. Grass, J. Braun, G. Borstel, R. Schneider, H. Dürr, Th. Fauster, and V. Dose, J. Phys.: Condens. Matter **5**, 599 (1993).

[46] S. H. Vosko, L. Wilk, and M. Nusair, Can. J. Phys. **58**, 1200 (1980).

[47] H. Ebert, in *Electronic Structure and Physical Properties of Solids*, edited by H. Dreyssé, Lecture Notes in Physics Vol. 535 (Springer, Berlin, 2000), p. 191.

[48] M. I. Katsnelson and A. I. Lichtenstein, Eur. Phys. J. B **30**, 9 (2002).

[49] L. V. Pourovskii, M. I. Katsnelson, and A. I. Lichtenstein, Phys. Rev. B **72**, 115106 (2005).

[50] S. Chadov, J. Minár, H. Ebert, A. Perlov, L. Chioncel, M. I. Katsnelson, and A. I. Lichtenstein, Phys. Rev. B **74**, 140411(R)

(2006).
[51] J. Braun, J. Minár, H. Ebert, M. I. Katsnelson, and A. I. Lichtenstein, Phys. Rev. Lett. **97**, 227601 (2006).
[52] M. Pickel, A. B. Schmidt, F. Giesen, J. Braun, J. Minár, H. Ebert, M. Donath, and M. Weinelt, Phys. Rev. Lett. **101**, 066402 (2008).
[53] J. Sánchez-Barriga, J. Fink, V. Boni, I. Di Marco, J. Braun, J. Minár, A. Varykhalov, O. Rader, V. Bellini, F. Manghi, H. Ebert, M. I. Katsnelson, A. I. Lichtenstein, O. Eriksson, W. Eberhardt, and H. A. Dürr, Phys. Rev. Lett. **103**, 267203 (2009).
[54] A. B. Shick and O. N. Mryasov, Phys. Rev. B **67**, 172407 (2003).
[55] O. Gunnarsson, M. Jonson, and B. I. Lundqvist, Phys. Rev. B **20**, 3136 (1979).
[56] J. W. Cable and H. R. Child, Phys. Rev. B **1**, 3809 (1970).
[57] J. Kudrnovský, V. Drchal, and P. Bruno, Phys. Rev. B **77**, 224422 (2008).
[58] E. W. Plummer and W. Eberhardt, Phys. Rev. B **20**, 1444 (1979).
[59] G. Bozzolo, R. D. Noebe, J. Khalil, and J. Morse, Appl. Surf. Sci. **219**, 149 (2003).